7-2-2020

Tacky Elastomers to Enable Tear-Resistant and Autonomous Self-Healing Semiconductor Composites

Song Zhang
University of Southern Mississippi, song.zhang@usm.edu

Yu-Hsuan Cheng
National Taiwan University

Luke Galuska
University of Southern Mississippi

Anirban Roy
Bruker Corporation

Matthias Lorenz
Oak Ridge National Laboratory

See next page for additional authors

Title Tacky elastomers to enable tear resistant and autonomous self-healing semiconductor composites

Song Zhang, [†] Yu-Hsuan Cheng, [†] Luke Galuska, Anirban Roy, Matthias Lorenz, Beibei Chen, Shaochuan Luo, Yen-Ting Li, Chih-Chien Hung, Zhiyuan Qian, P. Blake J. St. Onge, Gage T. Mason, Lewis Cowen, Dongshan Zhou, Sergei I. Nazarenko, Robson F. Storey, Bob C. Schroeder, Simon Rondeau-Gagné, Yu-Cheng Chiu, Xiaodan Gu**

[†] equally contributed to the work

Song Zhang, Luke Galuska, Beibei Chen, Dr. Zhiyuan Qian, Prof. Sergei I. Nazarenko, Prof. Robson F. Storey, Prof. Xiaodan Gu

School of Polymer Science and Engineering, Center for Optoelectronic Materials and Device

The University of Southern Mississippi

Hattiesburg, MS 39406, USA

E-mail: xiaodan.gu@usm.edu

Yu-Hsuan Cheng, Yen-Ting Lee, Chih-Chien Hung, Prof. Yu-Cheng Chiu

Department of Chemical Engineering

Advanced Research Center for Green Materials Science and Technology

National Taiwan University of Science and Technology

Taipei 10617, Taiwan

Email: ycchiu@mail.ntust.edu.tw

Dr. Anirban Roy

Bruker Corporation

Goleta, CA 93117, USA

This is the author manuscript accepted for publication and has undergone full peer review but has not been through the copyediting, typesetting, pagination and proofreading process, which may lead to differences between this version and the Version of Record. Please cite this article as doi: 10.1002/adfm.202000663.

Dr. Matthias Lorenz

Center for Nanophase Materials Sciences

Oak Ridge National Laboratory

Oak Ridge, TN 37831, USA

Dr. Shaochuan Luo, Prof. Dongshan Zhou

Department of Polymer Science and Engineering, School of Chemistry and Chemical Engineering

Nanjing University

Nanjing 210093, China

Lewis Cowen, Dr. Bob C. Schroeder

Department of Chemistry

University College London

London WC1H 0AJ, UK

P. Blake J. St. Onge, Gage T. Mason, Prof. Simon Rondeau-Gagné

Department of Chemistry and Biochemistry

University of Windsor

Ontario, N9B3P4, Canada

Keywords: (crack resistance, semiconducting polymers, autonomous self-healing, air-stable devices)

Mechanical failure of π-conjugated polymer thin films is unavoidable under cyclic loading conditions, due to intrinsic defects and poor resistance to crack propagation. Here, the first tear-resistant and room-temperature self-healable semiconducting composites is presented, consisting of conjugated polymers and butyl rubber elastomers. This new composite displays both record-low elastic modulus (< 1 MPa) and ultra-high deformability with fracture strain above 800%. More importantly, failure behavior is not sensitive to precut notches under deformation. Autonomous self-healing at room temperature, both mechanical and electronic, is demonstrated through physical contact of two separate films. The composite film also shows device stability in the ambient environment over five months due to much-improved barrier property to both oxygen and water. Butyl rubber is broadly applicable to various P-type and N-type semiconducting polymers for fabricating self-healable electronics to provide new resilient electronics that mimic the tear resistance and healable property of human skin.

1. Introduction

Decades of development of new organic semiconductors has boosted electronic performance (e.g. charge carrier mobility) to be comparable to their inorganic counterparts, like amorphous silicon.[1–5] Semiconducting polymers are known for their chemical tunability, solution processability, and mechanical deformability, which makes them promising candidates for flexible or deformable electronic devices.[6–9] In the past, researchers have focused on engineering semiconducting polymers with lower elastic modulus and maximized deformability through modifying their molecular structures, for example, through backbone/side-chain engineering, and introduction of cross-linkable moieties to polymer side chains and/or intermolecular hydrogen bonding to the backbone/side chain.[6,10–16] However, the mechanical performance of fully conjugated semiconducting polymers is limited due to their intrinsic rigid backbone and synthetically limited molecular weight, leading to a generally high elastic modulus (> 100 MPa) as compared to human skin (e.g. ~ 0.1 MPa), low deformability (< 200% of strain) and strong hysteresis under cyclic stretching.[6,8,17,18] This causes a great mismatch in mechanical properties between the wearable device and human skin. The buckling and delamination of the thin film device from soft skin can potentially be an issue.

Another promising method to achieve both high electrical and mechanical properties for a given semiconducting polymer is through physical blending with mechanically soft and deformable elastomers.[19–27] A blend of poly(3-hexylthiophene) (P3HT) and styrene-ethylene-butylene-styrene (SEBS) elastomer showed a relatively low charge transport mobility around 2×10^{-3} cm^2 V^{-1} s^{-1} at 50% strain, with a high fracture strain around 300%.[19] Similarly, commercially available crosslinked polydimethylsiloxane (PDMS) elastomer (Sylgard 184) has also been used as the elastomer matrix in semiconducting polymer blend systems.[22] Xu *et al.* introduced a conjugated polymer/elastomer phase separation-induced elasticity (CONPHINE) method to blend different polydiketopyrrolopyrrole

(PDPP)-based conjugated polymers with SEBS, thereby obtaining a high and stable charge mobility above 1 cm^2 V^{-1} s^{-1} under 100% strain.[23] Most recently, polystyrene-block-polyisoprene-block-polystyrene (SIS) and Triton X-100 were introduced to conjugated polymer blends for achieving self-healing performance.[28,29] However, the maximum deformability of these early composites was restricted due to limited ultimate strain of the elastomer component: 300% strain for pristine SEBS and 400% strain for pristine PDMS.[19] Even for systems with a highly extensive elastomeric phase, failure of the conjugated polymer phase is hard to avoid due to the rapid propagation of intrinsic defects during the tensile drawing at stress concentrated point near the crack tip. In order to achieve mechanically and electronically robust composite, it is necessary to substantially suppress crack initiation and propagation, together with healing of the crack region; thus a tear-resistant and self-healable polymeric semiconductor material is required.[30–32]

2. Result and Discussion

In this study, we report a new semiconducting composite using butyl rubber (BR) as the elastomer matrix due to its outstanding elasticity (low persistence length of 5.2 Å), strong adhesion and excellent barrier properties to both oxygen and water.[33] We hypothesize these properties will endow new performances to conjugated polymer composite system, such as resistance to crack propagation, self-healing property, and ambient-stability. A p-type donor-acceptor (D-A) semiconducting polymer, poly(2,5-bis(2-decyltetradecyl)-3,6-di(thiophen-2-yl)diketopyrrolo[3,4-c]pyrrole-1,4-dione-*alt*-thienovinylthiophene (PDPPTVT) was chosen as a model system for the demonstration of our concept of fracture resistant and healable composite film, owing to its high charge transport mobility (**Figure 1**a, 1b and Supplementary Table S1).[34] The blend ratio between donor polymers and elastomer matrix is critical for device morphology, and consequently device performance. To optimize the blend ratio between PDPPTVT and BR, we first measured the mechanical properties of the composite film with a pseudo-free standing tensile tester, where a dog-bone shaped thin film (60 nm) was prepared and stretched at a strain rate of 0.125 s^{-1} uniaxially on

top of a water surface.[35,36] As the fraction of BR was increased, the semiconducting polymer composite showed a significant drop in elastic modulus and great improvement in crack onset strain, especially when the BR phase became the continuous phase, above a weight fraction of about 50% (Figure 1c, 1d and Supplementary Table S2). In contrast to the low deformability of pristine PDPPTVT film, the composite film with a blend weight ratio of 1:8.5 for conjugated polymer:elastomer exhibited a record-low modulus of 1 MPa and record-high fracture strain exceeding 800%, which was shown to deform into a high aspect ratio polymer fiber under uniaxial loading (Supplementary Figure. S1 and Video S1, S2). Figure 1e compared the current system to several recently reported highly deformable and soft fully conjugated polymers (open symbol), non-conjugated polymers (half-filled symbol), and polymer composites (filled symbol); the data clearly demonstrate the outstanding mechanical performance for the current system, which displays the lowest modulus and highest deformability of all systems (Supplementary Table S3).[10,12,19,23,37–42]

Next, we demonstrated the tear-resistance of the new composite film using edge-notched dog-bone-shaped thin film samples with a notch size that is one third of the original width (2 mm). As expected, the notched pristine PDPPTVT broke at a very early stage. At a low BR content (33% weight fraction), the notch of composite film propagated quickly, leading to catastrophic fracture of the composite film below 25% strain (Supplementary Figure. S2a and Video S3); however, the notched 2:3 composite film withstood 50% strain, with the notch becoming quickly blunted and propagating slowly (Figure 1a). For 1:3 and 1:8.5 blend ratios, thin films did not fail even at 100% strain (Supplementary Figure. S2b-c). This observation was attributed to an ideal morphology with BR as the continuous matrix phase, low T_g and highly entangled BR network. Upon uniaxial loading, BR polymer chains were likely to align along the loading direction and redistribute the stress at the notch tip, thus the crack propagation was hindered. In the meantime, highly entangled BR polymer chains could resist the chain slippage and scission through intertwined polymer chains, thus preventing the system from catastrophic failure at the pre-cut notch.[43] To further highlight the

unique crack-resistance of BR, a control sample was fabricated using a pre-notched PDPPTVT/PDMS composite film at 1:3 blend ratio. This PDMS-based control showed rapid crack propagation and film failure at < 25% strain (Supplementary Figure. S2d). The results above showed that highly flexible BR can greatly improve the mechanical property of the conjugated polymer, enabling the composite film to achieve a record-high crack on-set strain, record-low elastic modulus, and outstanding tear resistance behavior.

The electrical performance of the composite film was also investigated through the fabrication of thin film organic field-effect transistors (OFETs). Shown in Figure 1f, the charge carrier mobility of thin films at different blend ratio was between 0.5 and 1.5 $cm^2 V^{-1} s^{-1}$ (Supplementary Figure. S3-S4 and Table S4). The relative insensitivity of charge carrier mobility to PDPPTVT/BR blend ratios can be understood through the unique fibril morphologies dispersed in the elastomer matrix as discussed later. Next, we performed strain-dependent electrical property measurements for both of 1:3 and 1:8.5 PDPPTVT/BR composite films, following a previously reported transfer method.[6] The thin film was first transferred onto the PDMS substrate and stretched to a desired strain before fabricating into an OFET device on a heavy doped Si substrate with a 300 nm SiO_2 gate dielectric layer. The mobility stayed within the same order of magnitude upon 150% strain along two charge transport directions (e.g. from 0.12 to 0.06 $cm^2 V^{-1} s^{-1}$ for 1:3 composite film and from 0.16 to 0.12 $cm^2 V^{-1} s^{-1}$ for 1:8.5 composite film), demonstrating its strong strain-insensitive electrical performance (Figure 1g, Supplementary Figure. S5-S9 and Table S5-S6). Since the electrical performance of organic semiconductors typically degrades rapidly with the presence of oxygen and water, we also explored the stability under ambient environmental conditions of OFET devices made from the new composite films.[44,45] Both 1:3 and 1:8.5 PDPPTVT/BR composite films were tested under different degrees of strain (0%, 50% and 100%), and the charge carrier mobility showed limited degradation (within 40%) after being stored under ambient conditions for over 150 days (Figure 1h, Supplementary Figure. S10, S11). We attributed such performance to the excellent oxygen and

water barrier resistance of BR. When compared with pristine PDMS elastomer, the oxygen and water permeability of pristine BR were 3136 and 56 times lower, measured by gas diffusion test and dry cup test (ASTM D1653-13), respectively (Supplementary Table S7).

The self-healing performance of PDPPTVT/BR composite film was tested at room temperature through the pseudo-free-standing tensile tester (**Figure 2**a). Two pieces of 2:3 composite polymer thin films with a size of 4 mm (length) × 4.7 mm (width) × 60 nm (thickness) were fabricated and floated on water. They were firstly compressed at 20% strain, then left for two seconds before being stretched (Figure 2b and Supplementary Video S4). It is observed that the two films adhered to each other autonomously within seconds during compression; the healed film could be strained past its original length by nearly 150%. When subjected to an identical test, a PDPPTVT polymer control did not show any sign of self-healing performance due to the loss of adhesion force (Figure 2c and Supplementary Video S5). This observation indicated that BR matrix provides room temperature self-healing mechanically properties for ultrathin films. Furthermore, using the same 2:3 composite film, we demonstrated that the electrical property can be restored (healed), as shown in Figure 2d. The edges of two separate pieces of films were physically compressed on top of a water surface, followed by transferring the film onto a SiO_2 substrate for transistor testing. Through landing probes on different electrodes, the electrical properties of the following film areas were measured: within pristine films, within self-healed region, and across the self-healed region. Both SEM and AFM showed good contact of two films with similar morphology, along with well-defined self-healing boundaries (Figure 2e, 2f and Supplementary Figure. S12). The hole mobility for Film I, Film II, and healed region was 0.093, 0.088, and 0.084 $cm^2\ V^{-1}\ s^{-1}$, respectively (Supplementary Figure. S13 and Table S8). To observe the electrical properties across the whole self-healed region, the charge mobility was extracted purposely from Electrode 4 to Electrode 8, as illustrated in Figure 2d, a long channel length fully crossing the self-healing region; the data showed that charge mobility was maintained within the same order of magnitude, averaging 0.043 $cm^2\ V^{-1}\ s^{-1}$.[46] It is worth noting

that, the transfer curve trace from the self-healing region (Electrode 1 to Electrode 2) in Figure S14 displayed little resistance enhancement at OFF current (red line curve with bumpy traces in the range small voltage) because of the increased thickness by the adhesion of two films, while the negative shift in threshold voltage caused lower ON current at the gate voltage of - 60 V due to the effect of longer channel length (Film I to Film II, green line curve). Furthermore, the self-healed composite film was strained at 50% for 1 cycle, 50 cycles, 100 cycles and 500 cycles. AFM 3D images clearly showed intact self-healed regions, while the charge mobilities of all probed regions were kept on the same order of magnitude before and after strain (Figure 2g, Supplementary Figure. S15-S22 and Table S9-S12). These results verified that the composite film is self-healable both mechanically and electrically.

The observed self-healing performance results from the following three procedures: the compression of two separate films allows for close contact of both BR chains and PDPPTVT fibril; the tackiness of BR enables two films to attach with each other; the fast segmental motion of low T_g BR polymer chains under room temperature leads to the reconstruction of conjugated PDPPTVT polymer chains, thus they can come back into contact. Together with PDPPTVT chains in contact upon compression, the conducting pathway for intermolecular hopping is built. We performed additional test to replace one side of PDPPTVT/BR composite to the PDPPTVT/polystyrene film, and healing ability drop as evident from the supporting video S6. We want to note that using DPP/polystyrene on both side of the cut film did show any healing behavior. Compared with previously reported conjugated polymer/elastomer composites, the PDPPTVT/BR composite film discussed above is the softest and most deformable system with tear-resistant and self-healable performances reported to date.

To demonstrate the general applicability of this method to create self-healable films, poly(3-hexylthiophene) (P3HT) and P3HT/BR composite films were also prepared and compared for their room temperature self-healing ability. For the neat P3HT film, upon compressing between two

separate edges, the film did not heal itself, while the 2:3 composite film healed autonomously on the water surface upon close contact (Supplementary Figure. S23). For the 2:3 P3HT/BR composite film, similar morphologies of the self-healing boundary were shown when compared with non-strained films upon 50% strain for 500 stretching cycles, while the charge mobility was slightly affected (Supplementary Figure. S24-34 and Table S13-17). This illustrated the capability of the proposed method in introducing self-healable performance to other conjugated polymer systems.

To fully understand the observed mechanical and electrical properties of the semiconductor composite, detailed thermal and morphological studies were performed. The glass transition temperature of different blend ratios of thin films was determined by alternating current (AC)-chip calorimetry. Two clear transitions at -57 °C and 10 °C were observed, attributed to backbone transitions for BR and PDPPTVT, respectively (Supplementary Figure. S35).[47–49] The sub-room temperature T_g of BR directly contributed to the high polymer chain flexibility and mobility at the room temperature, leading to a record-low elastic modulus for the composite film. Additionally, the combined tackiness and fast chain mobility allows the polymer composite to heal autonomously at room temperature. Exploration of the thin film morphology for different blend ratios of PDPPTVT/BR began with chemical imaging on the film surface using atomic force microscopy in combination with infrared-spectroscopy (AFM-IR, Anasys nanoIR-3) (**Figure 3**a-k and Supplementary Figure. S36).[50] Through comparison of IR absorption spectra of the two component polymers, two distinct characteristic absorption wavelengths, 1664 cm^{-1} (C=O stretching vibration in amide) and 1462 cm^{-1} (CH_3 torsional vibration) respectively, were chosen to selectively distinguish between the PDPPTVT and BR phase, respectively (Figure 3b-c). Firstly, AFM tapping mode was applied to obtain the phase images (Figure 3d-g). Next, the IR laser with the characteristic wavelength was aligned and focused at the gold coated AFM tip for a second scan. Upon absorption of the characteristic IR light, a thermal expansion would occur in the corresponding polymer phase, which was recorded by the change of tapping frequency of AFM tip, while the specific location was marked by a color (the green

color for the PDPPTVT phase and red for the BR phase (Figure 3h-k)). Due to the similar surface energy of two polymer components (PDPPTVT and BR) and high aggregation tendency of PDPPTVT polymer chains, a hierarchical structure of PDPPTVT aggregates in BR matrix was formed at different blend ratios (Supplementary Figure. S37 and Table. S18). For 2:1 composite film, PDPPTVT formed micrometer size aggregates across the surface. As the BR content exceeded 50%, the size of aggregates was greatly reduced and a mesh-like network comprising of interpenetrating PDPPTVT fibrils started to appear together with sparsely dispersed large PDPPTVT aggregates. At 1:8.5 blend ratio, the large aggregates almost fully disappeared and well dispersed PDPPTVT fibrils were observed to be scattered across the film. Due to the high deformability of the fibril-like geometry, these findings line up well with the greatly improved fracture strain as well as the high electrical performance of the conjugated polymer composites even under a high fraction of BR. The phase separation behavior was further studied by resonant soft X-ray scattering (RSoXS) (Supplementary Figure. S38), an inverse phase characterization technique that is sensitive to chemical composition. For 2:1, 1:1 and 1:3 blend systems, two regions of interest were observed from the 1D scattering profile, including a phase separation size of greater than 600 nm and a much smaller phase separation size around 60 nm, corresponding to the distance between large PDPPTVT aggregates and small fibers, respectively; these observations indicated that the PDPPTVT formed a unique hierarchical structure. However, only the small-scale phase separation was observed for the 1:8.5 blend, which can be attributed to the absence of large PDPPTVT aggregates, as seen in the AFM-IR measurement (Figure 3g, 3k). Overall, AFM-IR showed that at high BR content, conjugated polymers are dispersed as individual fibril structure within the continuous BR matrix.

Vertical phase separation was probed by elemental mapping using time-of-flight secondary ion mass spectrometry (TOF-SIMS) along the film thickness direction, where $C_4H_3S^+$ and Si^+ were characteristic signals originating from PDPPTVT and the Si substrate, respectively (Figure 3l and Supplementary Figure. S39). At 2:1 ratio, PDPPTVT was shown to be mostly concentrated on the top

surface of the 50 nm thin film. As the weight percent of BR increased, PDPPTVT tended to become better dispersed in the polymer composite. For 1:8.5 composite film, PDPPTVT was evenly mixed across the thickness direction. This observation implied that a higher proportion of BR leads to better dispersion of PDPPTVT fibers, providing uniform film deformation and water/oxygen stability and resulting in greater deformability. The grazing-incidence wide angle X-ray scattering (GIWAXS) experiment further confirmed the stable charge carrier mobility of the composite film, showing that PDPPTVT maintained its crystallization ability in different composite films, as evidenced by the clear (100) lamellar peak in the out-of-plane direction and near-linear decrease of relative degree of crystallinity (RDoC) with increasing percentage of BR in the composite film (Figure 3m and Supplementary Figure. S40). Ultraviolet-visible (UV-Vis) spectroscopy demonstrated limited difference in these composite films except for an increase in the intensity of the 0-0 transition peak with increasing BR content, which demonstrates enhanced aggregation through phase separation while maintaining the crystallization ability (Supplementary Figure. S41 and Table S19). In summary, detailed morphological characterizations suggested that the composite film with a high blend ratio produced a continuous PDPPTVT fibrillar structures embedded in the BR matrix, resulting in excellent mechanical property and stable electrical performance. Additionally, morphological control of composites based on different processing methods including varying temperature and/or additive conditions are also promising and warrant future study along this line.[51]

In addition to the p-type DPP-based D-A polymers, the same blending method was applied to three well-known semiconducting polymers, P3HT, poly(2,5-bis(3-hexadecyllthiophen-2-yl)thieno[3,2-b]thiophene) (PBTTT) and an air-sensitive n-type polymer, poly{[N,N'-bis(2-octyldodecyl)naphthalene-1,4,5,8-bis(dicarboximide)-2,6-diyl]-alt-5,5'-(2,2'-bithiophene)} (PNDI(2OD)2T).[52,53] All three composite films demonstrated a dramatic improvement in mechanical performance (lower modulus, better deformability and crack-resistance) when using BR as the matrix phase (**Figure 4**a, 4b, Supplementary Figure. S42, S43 and Table S20). We also performed

strain-dependent electrical property measurements for 1:3 PNDI(2OD)2T/BR composite (Figure 4c). In addition, the charge transport properties of pristine PNDI(2OD)2T and the 1:3 PNDI(2OD)2T/BR composite films were tested in the ambient environment to further validate their superior oxygen/water stability. The mobility of pristine PNDI(2OD)2T dropped by 6 orders of magnitudes within 2h in air due to oxygen doping; in comparison, the 1:3 composite film was electronically stable for 2 months, even under 100% strain (Figure 4d, Supplementary Figure. S44, S45 and Table S21). The initial decrease in charge mobility of the pristine PNDI(2OD)2T presumably resulted from oxygen diffusion into the dielectric layer, which was significantly delayed by the existence of BR in the composite film.[54] These results illustrate that using BR as the elastomer matrix for deformable and healable composites can be widely applied to a variety of semiconducting polymers, especially those with known sensitivity to oxygen and/or water. On a broader scale, such method also shows a great potential in fabricating novel stretchable conductive nanocomposites.[55]

3. Conclusions

In summary, we have demonstrated the use of BR as a new matrix polymer for the preparation of semiconducting composites that display unprecedented mechanical and electrical performance, including record low modulus, record high deformability, and resistance to crack-propagation, as well as strain-insensitive electronic property, autonomous healable and ambient-stable charge carrier mobility for both n-type and p-type D-A polymers. Developing new elastomers for conjugated polymer composite can facilitate future developments towards more robust flexible and deformable electronics for wearable applications.

4. Experimental Section

Pseudo-free-standing Thin Film Tensile Test: Thin film tensile tests were performed on a water surface through pseudo-free-standing tensile tester. Details of the tensile stage setup can be found in our previous publication.[35] Briefly, the polymer thin films (~ 50 nm) were patterned into dog-

bone shape by ultra-fast laser patterning, floated on top of water, and unidirectionally deformed at a strain rate of 0.125 s^{-1} until film fracture. At least six independent specimens were measured for each sample to provide statistically averaged mechanical property. The elastic modulus was obtained from the slope of the linear fit of the elastic region of the stress-strain curve using the first 1% strain.

Device Fabrication and Characterization: FET devices were fabricated on highly doped n-type Si (100) wafers with octadecyltrimethoxysilane (OTS)-modified SiO_2 (capacitance per unit area Ci = 10 nF cm^{-2}). The organic semiconducting thin films were spun-cast on SiO_2/Si substrates at a spinning rate of 1000 rpm for 60 s from prepared polymer solutions in chlorobenzene (5 mg/ml) at 70 °C. The films were thermal annealed at 170 °C for 1 h inside a N_2-filled glove box. Top-contact gold electrodes (50 nm) were subsequently deposited by evaporation through a shadow mask with the channel length (L) and width (W) defined as 50 and 1000 µm, respectively. All the measurements of transistors were conducted using a Keithley 4200 semiconductor parameter analyzer (Keithley Instruments Inc., Cleveland, OH, USA) under dry N_2 (glove box) and ambient atmosphere at room temperature.

Atomic Force Microscopy with Nanoscale Infrared Spectroscopy (Nano-IR AFM): All measurements were performed using Bruker Anasys nanoIR3 system equipped with HyperSpectra QCL (800-1800 cm^{-1}) laser source. Tapping mode AFM and AFM-IR measurements were done with gold coated Si probes (PR-EX-TnIR-A probes, nominal diameter ~25 nm). For spectral measurements, data spacing was set to 4 cm^{-1}. Acquired spectra were smoothed using Savitzky-Golay (3,5) filter.

Oxygen and Water Vapor Permeability Measurements: The oxygen permeability of BR and PDMS films was measured at 23°C, 0% RH, and 1 atm partial oxygen pressure difference using a commercially manufactured diffusion apparatus OX-TRAN® 2/21 ML (MOCON). BR film with area of

50 cm² was tested using pure oxygen gas. PDMS film was masked with aluminum foil with inner hole size of 5 cm² and tested using 4% oxygen/nitrogen to avoid the saturation of oxygen sensor. The oxygen transmission rate of PDMS was then normalized to 100% O_2. The permeability of oxygen for BR and PDMS films was determined as 1.753 and 5498.0 cc·cm/(m^2·day·atm) respectively. Water vapor permeability test of both BR and PDMS films was conducted via dry cup test (ASTM D1653 – 13) in a humidity chamber at 20°C and 94% relative humidity.

Time-of-flight Secondary Ion Mass Spectrometry (TOF-SIMS): TOF-SIMS experiments were performed on an IONTOF TOF.SIMS 5 platform (IONTOF GmbH, Münster, Germany), equipped with a 30 keV maximum energy bismuth liquid metal ion source (LMIS) and an argon gas cluster ion source (GCIS). The instrument was used for dual beam depth profiling with a Bi_3^+ analysis beam (0.48 nA DC beam current) and a 10 keV Ar_{2550}^+ sputter beam (68 pA beam current). The LMIS was operated in Fast Imaging mode to enable high lateral resolution chemical imaging at nominal mass resolution. Depth profiles were acquired in positive ion mode with non-interlaced cycles of 2 analysis frames (128×128 pixels, random scan pattern, 25 µm × 25 µm) and 1 sputter frame (800 µm × 800 µm). The depth profiling data sets were cropped to 19 µm × 19 µm lateral dimensions and integrated over one spatial dimension for the 2D representation in Figures 3l and S39.

Resonant Soft X-ray Scattering (RSoXS): RSoXS data was collected at beamline 11.0.1.2 of the Advanced Light Source, Lawrence Berkeley National Laboratory. X-ray energy of 286.8 eV was chosen based on Near Edge X-ray Absorption Fine Structure (NEXAFS) spectroscopy for two individual components to maximize the scattering contrast between conjugated polymers and elastomer matrix. Scattering data were collected with a sample-to-detector distances of 150 mm to give a q range of 0.001–0.020 $Å^{-1}$. Data analysis was also performed using a modified Nika package supported in the Igor Pro environment.

Grazing Incidence Wide Angle X-ray Scattering (GIWAXS): Grazing incidence wide-angle X-ray scattering (GIWAXS) of conjugated polymer thin film was carried out at the Stanford Synchrotron Radiation Lightsource (SSRL) on beamline 11-3. Data were collected under helium environment with an incident beam energy at 12.7 keV and an incidence angle of 0.12°. The sample to detector distance was about 250 mm. Diffraction data analysis was performed using Nika software package for Wavemetrics Igor, in combination with WAXStools. The relative degree of crystallinity (RDoC) was calculated through pole figure analysis followed by previously reported methods.[56]

UV-Vis-NIR Absorption Spectroscopy: The UV-Vis-NIR spectra for composite films were recorded on Agilent Cary 5000 using polymer thin films deposited on glass slides.

Alternating Current (AC) Chip Calorimetry: The glass transition temperature of the polymeric thin film was measured by an AC chip calorimeter. Thin film samples were floated off a Si substrate and then transferred to the sensor XI392 (Xensor integrations, NL), containing a large smooth heated area (100 μm × 100 μm). The experiments were performed at a frequency of 10 Hz and a heating/cooling rate of 1 °C/min. Each sample was scanned three times under a protecting nitrogen atmosphere. The amplitude of the complex differential voltage as a function of measuring temperature was obtained. The glass transition temperature was determined as the half-step temperature of the amplitude as previous reported.[47]

Differential Scanning Calorimetry (DSC): DSC measurement of PDPPTVT was performed on Mettler-Toledo DSC 3+ equipped with FRS 6+ sensor. Dry nitrogen gas with a flow rate of 50 ml/min was used as inert atmosphere. Heat-cool-heat cycle with heating/cooling rate of 30 °C/min was applied to enhance the thermal transition signal. In addition, physical aging experiment was carried out at -10 °C for 2 hrs for the confirmation of T_g around 17 °C.

Supporting Information

Supplementary information (pdf)

Supplementary video 1

Supplementary video 2

Supplementary video 3

Supplementary video 4

Supplementary video 5

Supplementary video 6

Conflict of Interest

The authors declare no conflict of interest.

Acknowledgements

This work was supported by USM faculty start-up funding and partially supported by the U.S. Department of Energy, Office of Science, Office of Basic Energy Science under award number of DE-SC0019361. L.G. thanks financial support from National Science Foundation Division of Graduate Education (DGE - 1449999). Y. H. C, Y. T. L, C. C. H. and Y. C. C thank financial support from "Advanced Research Center for Green Materials Science and Technology" from The Featured Area Research Center Program within the framework of the Higher Education Sprout Project by the Ministry of Education (108L9006) and the Ministry of Science and Technology in Taiwan (MOST 108-3017-F-002-002 and 108-2221-E-011-047). S.L. and D.Z. thank National Science Foundation of China (#21790345) for providing funding to support the AC-chip DSC test. S.R.-G. thanks the Natural Sciences and Engineering Research Council of Canada (NSERC) for financial support through a Discovery Grant (RGPIN-2017-06611). B.C. and S.N. thank the US National Science Foundation (CHM - #1807096) for providing partial support for gas transport measurement. L.C. acknowledges financial support from the EPSRC (EP/N509577/1) and B.S. from the Royal Society (RG/R2/180437). Use of the Stanford Synchrotron Radiation Lightsource (SSRL), SLAC National Accelerator Laboratory, is supported by the U.S. Department of Energy, Office of Science, Office of Basic Energy Sciences under Contract No. DE-AC02-76SF00515. This research used resources of the Advanced Light Source, which is a DOE Office of Science User Facility under contract no. DE-AC02-05CH11231. Part of this research was conducted at the Center for Nanophase Materials Sciences, which is a DOE Office of Science User Facility, using instrumentation within ORNL's Materials Characterization Core provided by UT-Battelle, LLC under Contract No. DE-AC05-00OR22725 with the U.S. Department of Energy. We thank Dr. Nikolay Borodinov, Dr. Alison Pawlicki for helpful discussion on the AFM-IR, and Dr. Cheng Wang for his assistance for the RSoXs measurement, Tim J. Dunn for assistance of the GIWAXS experiment set-up, and Prof. Derek L. Patton for the access of contact angle goniometer.

Received: ((will be filled in by the editorial staff))
Revised: ((will be filled in by the editorial staff))
Published online: ((will be filled in by the editorial staff))

References

[1] R. Noriega, J. Rivnay, K. Vandewal, F. P. V. Koch, N. Stingelin, P. Smith, M. F. Toney, A. Salleo, *Nat. Mater.* **2013**, *12*, 1038.

[2] J. Mei, Y. Diao, A. L. Appleton, L. Fang, Z. Bao, *J. Am. Chem. Soc.* **2013**, *135*, 6724.

[3] A. F. Paterson, S. Singh, K. J. Fallon, T. Hodsden, Y. Han, B. C. Schroeder, H. Bronstein, M. Heeney, I. McCulloch, T. D. Anthopoulos, *Adv. Mater.* **2018**, *30*, 1801079.

[4] M. S. Vezie, S. Few, I. Meager, G. Pieridou, B. Dörling, R. S. Ashraf, A. R. Goñi, H. Bronstein, I. McCulloch, S. C. Hayes, M. Campoy-Quiles, J. Nelson, *Nat. Mater.* **2016**, *15*, 746.

[5] D. Venkateshvaran, M. Nikolka, A. Sadhanala, V. Lemaur, M. Zelazny, M. Kepa, M. Hurhangee, A. J. Kronemeijer, V. Pecunia, I. Nasrallah, I. Romanov, K. Broch, I. McCulloch, D. Emin, Y. Olivier, J. Cornil, D. Beljonne, H. Sirringhaus, *Nature* **2014**, *515*, 384.

[6] J. Y. Oh, S. Rondeau-Gagné, Y. C. Chiu, A. Chortos, F. Lissel, G. J. N. Wang, B. C. Schroeder, T. Kurosawa, J. Lopez, T. Katsumata, J. Xu, C. Zhu, X. Gu, W. G. Bae, Y. Kim, L. Jin, J. W. Chung, J. B. H. Tok, Z. Bao, *Nature* **2016**, *539*, 411.

[7] A. Chortos, J. Liu, Z. Bao, *Nat. Mater.* **2016**, *15*, 937.

[8] S. E. Root, S. Savagatrup, A. D. Printz, D. Rodriquez, D. J. Lipomi, *Chem. Rev.* **2017**, *117*, 6467.

[9] Z. Bao, X. Chen, *Adv. Mater.* **2016**, *28*, 4177.

[10] C. Müller, S. Goffri, D. W. Breiby, J. W. Andreasen, H. D. Chanzy, R. A. J. Janssen, M. M. Nielsen, C. P. Radano, H. Sirringhaus, P. Smith, N. Stingelin-Stutzmann, *Adv. Funct. Mater.* **2007**, *17*, 2674.

[11] Y. Zhao, J. Liu, X. Li, Y. Lu, S. Q. Wang, *Macromolecules* **2017**, *50*, 2024.

[12] G. J. N. Wang, L. Shaw, J. Xu, T. Kurosawa, B. C. Schroeder, J. Y. Oh, S. J. Benight, Z. Bao, *Adv. Funct. Mater.* **2016**, *26*, 7254.

[13] S. E. Root, M. A. Alkhadra, D. Rodriquez, A. D. Printz, D. J. Lipomi, *Chem. Mater.* **2017**, *29*, 2646.

[14] J. W. Mok, Z. Hu, C. Sun, I. Barth, R. Munoz, J. Jackson, T. Terlier, K. G. Yager, R. Verduzco, *Chem. Mater.* **2018**, *30*, 8314.

[15] G. J. N. Wang, Y. Zheng, S. Zhang, J. Kang, H. C. Wu, A. Gasperini, H. Zhang, X. Gu, Z. Bao, *Chem. Mater.* **2018**.

[16] Y. Zheng, G. N. Wang, J. Kang, M. Nikolka, H. Wu, H. Tran, S. Zhang, H. Yan, H. Chen, P. Y. Yuen, J. Mun, R. H. Dauskardt, I. McCulloch, J. B. -H. Tok, X. Gu, Z. Bao, *Adv. Funct. Mater.* **2019**, 1905340.

[17] S. Zhang, M. U. Ocheje, L. Huang, L. Galuska, Z. Cao, S. Luo, Y. H. Cheng, D. Ehlenberg, R. B. Goodman, D. Zhou, Y. Liu, Y. C. Chiu, J. D. Azoulay, S. Rondeau-Gagné, X. Gu, *Adv. Electron. Mater.* **2019**, *5*, 1800899.

[18] H. Joodaki, M. B. Panzer, *Proc. Inst. Mech. Eng. Part H J. Eng. Med.* **2018**, *232*, 323.

[19] M. Shin, J. Y. Oh, K. E. Byun, Y. J. Lee, B. Kim, H. K. Baik, J. J. Park, U. Jeong, *Adv. Mater.* **2015**, *27*, 1255.

[20] H. J. Kim, A. Thukral, S. Sharma, C. Yu, *Adv. Mater. Technol.* **2018**, *3*, 1800043.

[21] D. Choi, H. Kim, N. Persson, P. H. Chu, M. Chang, J. H. Kang, S. Graham, E. Reichmanis, *Chem. Mater.* **2016**, *28*, 1196.

[22] E. Song, B. Kang, H. H. Choi, D. H. Sin, H. Lee, W. H. Lee, K. Cho, *Adv. Electron. Mater.* **2016**, *2*, 1500250.

[23] J. Xu, S. Wang, G. J. N. Wang, C. Zhu, S. Luo, L. Jin, X. Gu, S. Chen, V. R. Feig, J. W. F. To, S. Rondeau-Gagné, J. Park, B. C. Schroeder, C. Lu, J. Y. Oh, Y. Wang, Y. H. Kim, H. Yan, R. Sinclair, D. Zhou, G. Xue, B. Murmann, C. Linder, W. Cai, J. B. H. Tok, J. W. Chung, Z. Bao, *Science.* **2017**, *355*, 59.

[24] D. C. Kim, H. J. Shim, W. Lee, J. H. Koo, D. Kim, *Adv. Mater.* **2019**, *0*, 1902743.

[25] J. Xu, H. C. Wu, C. Zhu, A. Ehrlich, L. Shaw, M. Nikolka, S. Wang, F. Molina-Lopez, X. Gu, S. Luo, D. Zhou, Y. H. Kim, G. J. N. Wang, K. Gu, V. R. Feig, S. Chen, Y. Kim, T. Katsumata, Y. Q. Zheng, H. Yan, J. W. Chung, J. Lopez, B. Murmann, Z. Bao, *Nat. Mater.* **2019**, *18*, 594.

[26] S. Goffri, C. Müller, N. Stingelin-Stutzmann, D. W. Breiby, C. P. Radano, J. W. Andreasen, R. Thompson, R. A. J. Janssen, M. M. Nielsen, P. Smith, H. Sirringhaus, *Nat. Mater.* **2006**, *5*, 950.

[27] T. Sun, J. I. Scott, M. Wang, R. J. Kline, G. C. Bazan, B. T. O'Connor, *Adv. Electron. Mater.* **2017**, *3*, 1600388.

[28] S. Kee, M. A. Haque, D. Corzo, H. N. Alshareef, D. Baran, *Adv. Funct. Mater.* **2019**, *29*, 1905426.

[29] Y. J. Jeong, J. Jung, E. H. Suh, D. J. Yun, J. G. Oh, J. Jang, *Adv. Funct. Mater.* **2020**, *30*, 1905809.

[30] W. Yang, V. R. Sherman, B. Gludovatz, E. Schaible, P. Stewart, R. O. Ritchie, M. A. Meyers, *Nat. Commun.* **2015**, *6*, 6649.

[31] J. Kang, J. B. H. Tok, Z. Bao, *Nat. Electron.* **2019**, *2*, 144.

[32] J. Y. Oh, D. Son, T. Katsumata, Y. Lee, Y. Kim, J. Lopez, H.-C. Wu, J. Kang, J. Park, X. Gu, J. Mun, N. G.-J. Wang, Y. Yin, W. Cai, Y. Yun, J. B. H. Tok, Z. Bao, *Sci. Adv.* **2019**, *5*, eaav3097.

[33] P. C. Hiemenz, T. P. Lodge, *Polymer chemistry*; CRC press, 2007.

[34] H. Chen, Y. Guo, G. Yu, Y. Zhao, J. Zhang, D. Gao, H. Liu, Y. Liu, *Adv. Mater.* **2012**, *24*, 4618.

[35] S. Zhang, M. U. Ocheje, S. Luo, D. Ehlenberg, B. Appleby, D. Weller, D. Zhou, S. Rondeau-Gagné, X. Gu, *Macromol. Rapid Commun.* **2018**, *39*, 1800092.

[36] Y. Liu, Y. C. Chen, S. Hutchens, J. Lawrence, T. Emrick, A. J. Crosby, *Macromolecules* **2015**, *48*, 6534.

[37] Y. Li, W. K. Tatum, J. W. Onorato, S. D. Barajas, Y. Y. Yang, C. K. Luscombe, *Polym. Chem.* **2017**, *8*, 5185.

[38] H. F. Wen, H. C. Wu, J. Aimi, C. C. Hung, Y. C. Chiang, C. C. Kuo, W. C. Chen, *Macromolecules* **2017**, *50*, 4982.

[39] B. O'Connor, E. P. Chan, C. Chan, B. R. Conrad, L. J. Richter, R. J. Kline, M. Heeney, I. McCulloch, C. L. Soles, D. M. DeLongchamp, *ACS Nano* **2010**, *4*, 7538.

[40] H. C. Wu, C. C. Hung, C. W. Hong, H. S. Sun, J. T. Wang, G. Yamashita, T. Higashihara, W. C. Chen, *Macromolecules* **2016**, *49*, 8540.

[41] F. Sugiyama, A. T. Kleinschmidt, L. V. Kayser, M. A. Alkhadra, J. M. H. Wan, A. S. C. Chiang, D. Rodriquez, S. E. Root, S. Savagatrup, D. J. Lipomi, *Macromolecules* **2018**, *51*, 5944.

[42] R. Peng, B. Pang, D. Hu, M. Chen, G. Zhang, X. Wang, H. Lu, K. Cho, L. Qiu, *J. Mater. Chem. C* **2015**, *3*, 3599.

[43] B. Huneau, *Rubber Chem. Technol.* **2011**, *84*, 425−452.

[44] Y. W. Soon, S. Shoaee, R. S. Ashraf, H. Bronstein, B. C. Schroeder, W. Zhang, Z. Fei, M. Heeney, I. McCulloch, J. R. Durrant, *Adv. Funct. Mater.* **2014**, *24*, 1474.

[45] M. L. Chabinyc, F. Endicott, B. D. Vogt, D. M. DeLongchamp, E. K. Lin, Y. Wu, P. Liu, B. S. Ong, *Appl. Phys. Lett.* **2006**, *88*, 113514.

[46] P. Mittal, B. Kumar, Y. S. Negi, B. K. Kaushik, R. K. Singh, *Microelectronics J.* **2012**, *43*, 985.

[47] D. Zhou, H. Huth, Y. Gao, G. Xue, C. Schick, *Macromolecules* **2008**, *41*, 7662.

[48] C. Zou, N. Yanahashi, Y. Wu, J. Wang, C. Zhang, G. Xiong, H. Yang, L. Jiang, T. Ikeda, *Adv. Funct. Mater.* **2019**, *29*, 1804838.

[49] Z. Qian, Z. Cao, L. Galuska, S. Zhang, J. Xu, X. Gu, *Macromol. Chem. Phys.* **2019**, *220*, 1900062.

[50] K. L. Gu, Y. Zhou, W. A. Morrison, K. Park, S. Park, Z. Bao, *ACS Nano* **2018**, *12*, 1473.

[51] S. Choi, S. I. Han, D. Jung, H. J. Hwang, C. Lim, S. Bae, O. K. Park, C. M. Tschabrunn, M. Lee, S. Y. Bae, J. W. Yu, J. H. Ryu, S. W. Lee, K. Park, P. M. Kang, W. B. Lee, R. Nezafat, T. Hyeon, D. H. Kim, *Nat. Nanotechnol.* **2018**, *13*, 1048.

[52] I. McCulloch, M. Heeney, C. Bailey, K. Genevicius, I. MacDonald, M. Shkunov, D. Sparrowe, S. Tierney, R. Wagner, W. Zhang, M. L. Chabinyc, R. J. Kline, M. D. McGehee, M. F. Toney, *Nat. Mater.* **2006**, *5*, 328.

[53] H. Yan, Z. Chen, Y. Zheng, C. Newman, J. R. Quinn, F. Dötz, M. Kastler, A. Facchetti, *Nature* **2009**, *457*, 679.

[54] J. T. E. Quinn, J. Zhu, X. Li, J. Wang, Y. Li, *J. Mater. Chem. C* **2017**, *5*, 8654.

[55] S. Choi, S. I. Han, D. Kim, T. Hyeon, D. H. Kim, *Chem. Soc. Rev.* **2019**, *48*, 1566.

[56] J. L. Baker, L. H. Jimison, S. Mannsfeld, S. Volkman, S. Yin, V. Subramanian, A. Salleo, A. P. Alivisatos, M. F. Toney, *Langmuir* **2010**, *26*, 9146.

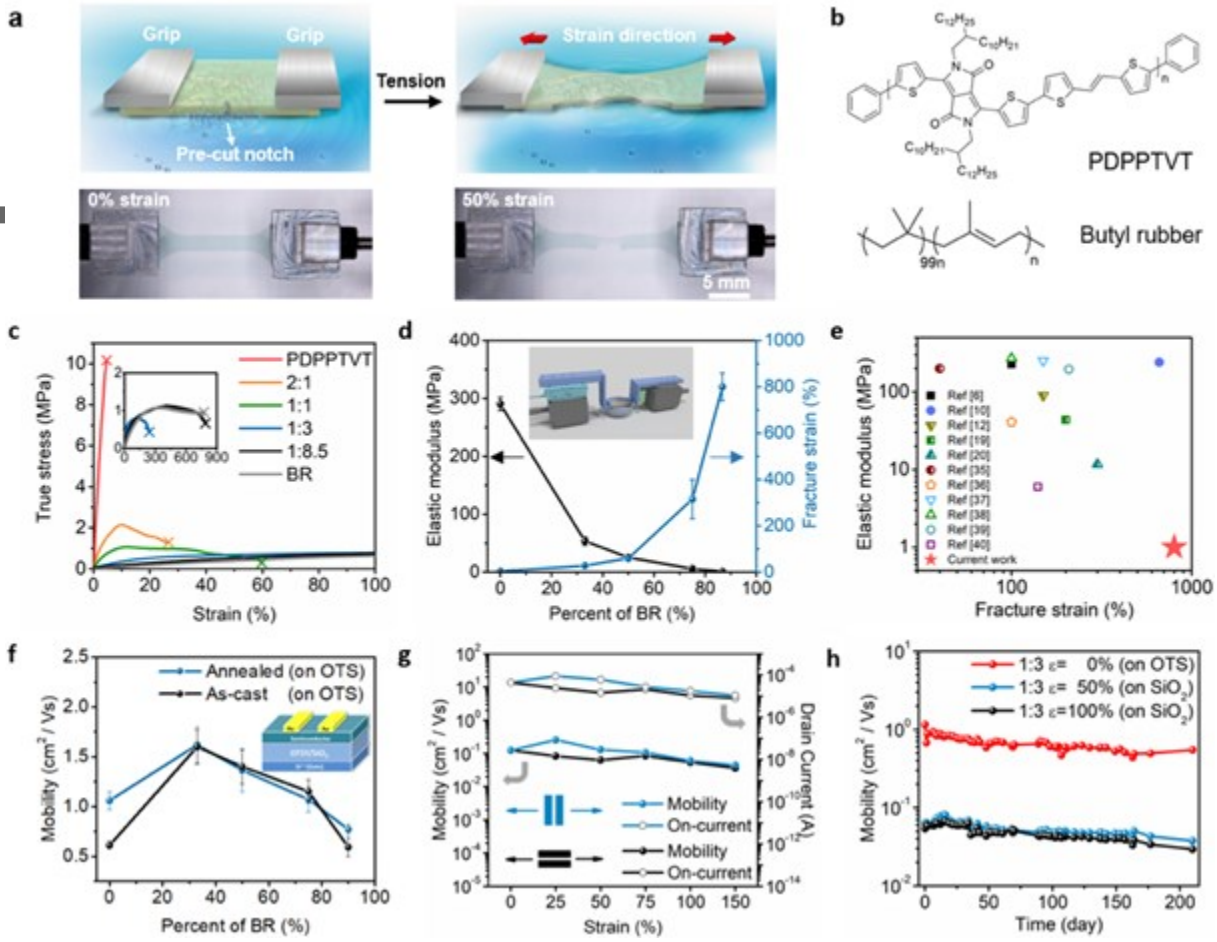

Figure 1. Mechanical and electrical performances for PDPPTVT/BR composite film. (a) 3D schematic illustration and optical images of notched 2:3 PDPPTVT/BR composite film before and after tensile deformation on water surface. (b) Chemical structures for PDPPTVT and BR. (c) Stress-strain curves for different blend ratios of PDPPTVT/BR. Inset: Stress-strain curves for 1:3 and 1:8.5 blend. (d) Elastic modulus and crack onset strain for different blend ratios of PDPPTVT/BR. The inset shows the scheme of tensile testing setup. (e) Comparison of the mechanical performance of the current system to previously reported semiconducting polymeric materials. (f) Charge carrier mobility of OFET devices made using different blend ratios of PDPPTVT/BR. (g) Charge carrier mobility and drain current of 1:3 PDPPTVT/BR composite film upon stretching in parallel and in perpendicular to charge transfer direction at different strain without annealing. (h) Time-dependent charge mobility of OFET devices for 1:3 PDPPTVT/BR composite films.

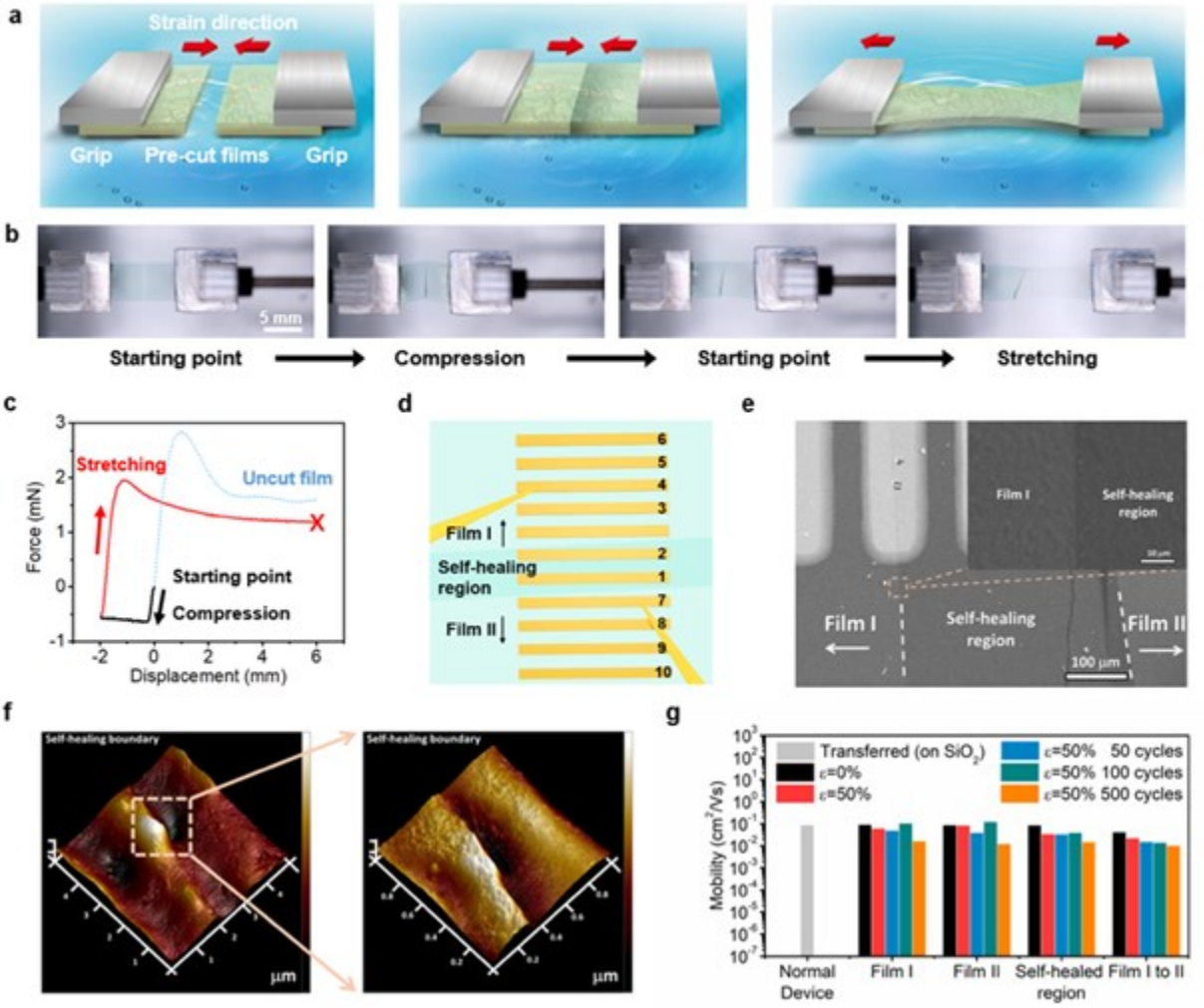

Figure 2. Characterization of self-healing behavior for PDPPTVT/BR semiconducting composites. (a) 3D schematic demonstrating the self-healing process. Two pre-cut films were floated on water upon compression. (b) Optical images of self-healing behavior for 2:3 PDPPTVT/BR composite film. Two films were first compressed at 20% to allow adhesion and later immediately stretched for 150% of the original length (4mm). (c) Force-displacement plot of 2:3 PDPPTVT/BR composite film during deformation process as described in (b). The blue curve shows the tensile test result of an uncut film for comparison. (d) Schematic illustration of the OFET device fabricated by self-healed film. (e) SEM image on the self-healable region of the OFET device. (f) AFM 3D images showing the self-healing boundary of 2:3 PDPPTVT/BR film. (g) Summary of charge carrier mobility for self-healed 2:3 PDPPTVT/BR composite films measured at different electrodes before and after strain for various cycles.

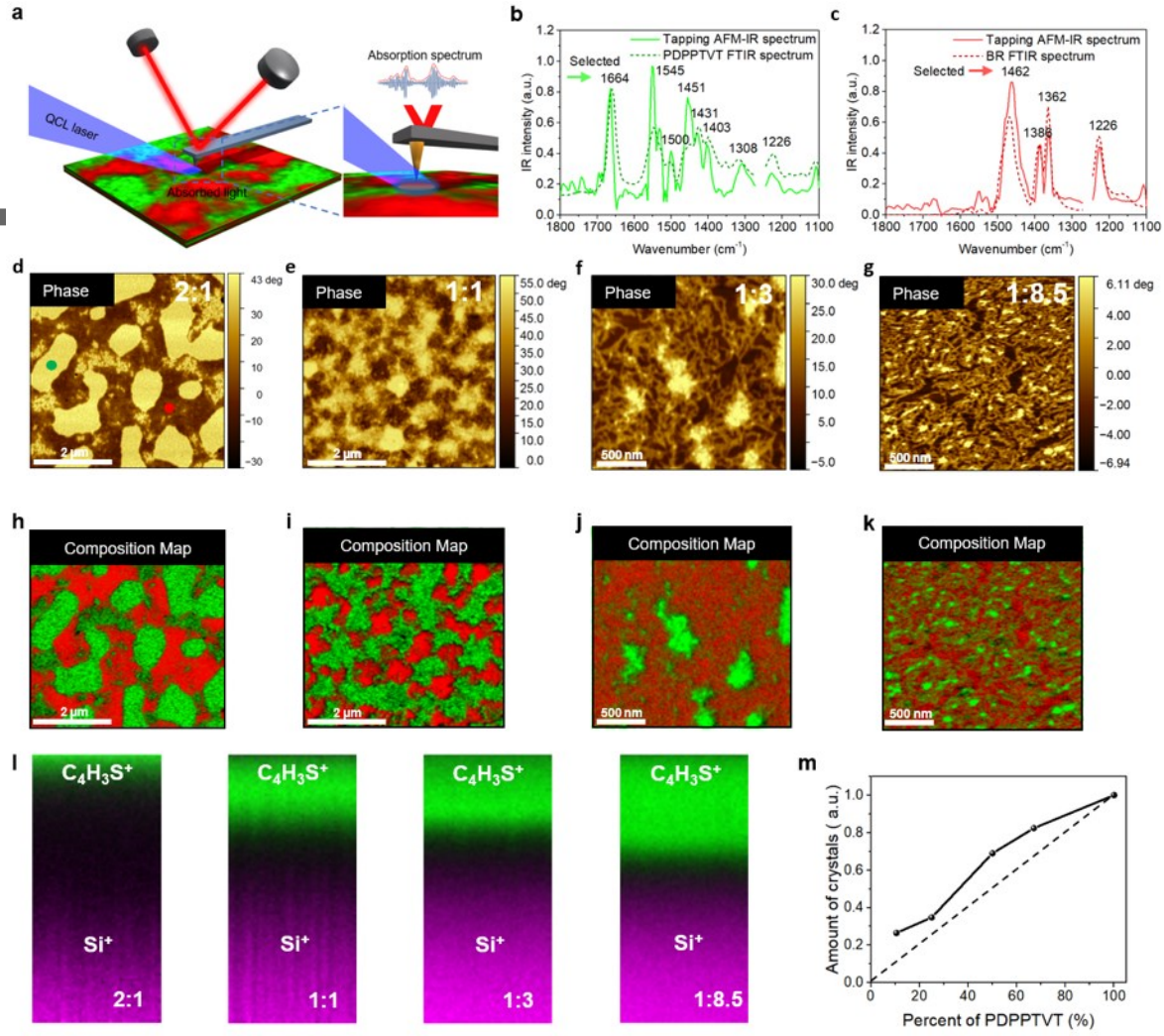

Figure 3. Morphological characterization of different blend ratios of PDPPTVT/BR systems. (a-k) Nano IR-AFM test. (a) 3D schematic of the working principle for the IR-AFM system. (b, c) IR absorption spectrum of PDPPTVT and BR polymer taken by the IR-AFM and FTIR. The characteristic IR absorption peaks selected for PDPPTVT and BR are 1664 cm^{-1} and 1462 cm^{-1}, respectively, as shown by the arrow. (d-g) AFM phase images for different blend ratios of PDPPTVT/BR composite film. (h-k) IR-AFM overlay images highlighting the distributions of PDPPTVT and BR (green color represents for PDPPTVT at 1664 cm^{-1} and red color represents for BR at 1462 cm^{-1}). (l) TOF-SIMS chemical depth profiling overlay (19 μm lateral field of view × 200 erosion frames) for samples with different blend ratios of PDPPTVT/BR composite film. The composition of $C_4H_3S^+$ (from PDPPTVT) is marked with green color and Si^+ (from Si wafer) is marked with purple color. (m) Relative degree of crystallinity for different blend ratios of PDPPTVT-BR based on (100) lamellar peak.

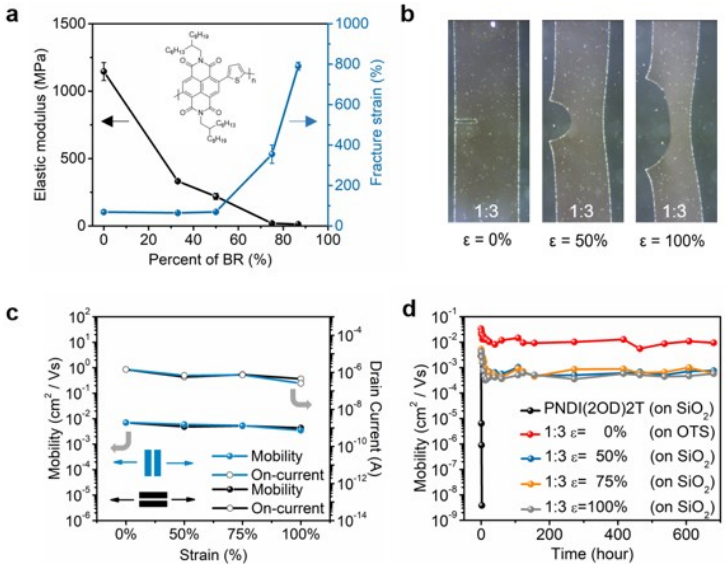

Figure 4. Mechanical and electrical performance of PNDI(2OD)2T/BR composite films. (a) Elastic modulus and crack onset strain for different blend ratios of PNDI(2OD)2T/BR. (b) Optical images of notched 1:3 composite film under stretching at different degrees of strain. (c) Charge carrier mobility and drain current of OFET devices made by 1:3 ratio of PNDI(2OD)2T/BR blend system under various degrees of strain. (d) Time-dependent charge mobility of OFET devices for 1:3 ratio PNDI(2OD)2T/BR blend system under various degrees of strain.

A mechanically durable and electronically stable semiconducting composite is engineered through introducing a blend of donor-acceptor polymer and butyl rubber elastomer. The composite exhibits ultra-low modulus, ultra-high deformability, tear-resistance and self-healing performance, as well as ambient-stable device stability. This method is widely applicable to different semiconducting polymers.

Keyword (semiconducting polymers)

Song Zhang, [†] Yu-Hsuan Cheng, [†] Luke Galuska, Anirban Roy, Matthias Lorenz, Beibei Chen, Shaochuan Luo, Yen-Ting Li, Chih-Chien Hung, Zhiyuan Qian, P. Blake J. St. Onge, Gage T. Mason, Lewis Cowen, Dongshan Zhou, Sergei I. Nazarenko, Robson F. Storey, Bob C. Schroeder, Simon Rondeau-Gagné, Yu-Cheng Chiu*, Xiaodan Gu*

Title Tacky elastomers to enable tear resistant and autonomous self-healing semiconductor composites

ToC figure